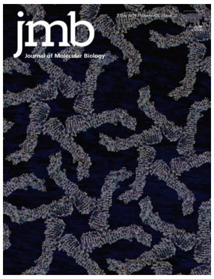

Cryo-EM Analysis Reveals Structural Basis of *Helicobacter pylori* VacA Toxin Oligomerization

Min Su [1,†], Amanda L. Erwin [1,2,†], Anne M. Campbell [3], Tasia M. Pyburn [4], Lauren E. Salay [5], Jessica L. Hanks [1], D. Borden Lacy [6,7], David L. Akey [1], Timothy L. Cover [3,6,7] and Melanie D. Ohi [1,2]

*1 - **Life Sciences Institute,** University of Michigan, Ann Arbor, MI 48109, USA*
*2 - **Department of Cell and Developmental Biology,** University of Michigan, Ann Arbor, MI 48109, USA*
*3 - **Department of Medicine,** Vanderbilt University School of Medicine, Nashville, TN 37212, USA*
*4 - **Department of Cell and Developmental Biology,** Vanderbilt University, Nashville, TN 37212, USA*
*5 - **Department of Biochemistry,** Vanderbilt University School of Medicine, Nashville, TN 37212, USA*
*6 - **Department of Pathology,** Microbiology, and Immunology, Vanderbilt University School of Medicine, Nashville, TN 37212, USA*
*7 - **Veterans Affairs Tennessee Valley Healthcare System,** Nashville, TN 37212, USA*

***Correspondence to Timothy L. Cover and Melanie D. Ohi:** Department of Medicine, Vanderbilt University School of Medicine, Nashville, TN 37212, USA Life Sciences Institute, 210 Washtenaw Avenue, Ann Arbor, MI 48109-2216, USA. timothy.l.cover@vanderbilt.edu, mohi@umich.edu.*

https://doi.org/10.1016/j.jmb.2019.03.029
Edited by Karolin Luger

Abstract

Helicobacter pylori colonizes the human stomach and contributes to the development of gastric cancer and peptic ulcer disease. *H. pylori* secretes a pore-forming toxin called vacuolating cytotoxin A (VacA), which contains two domains (p33 and p55) and assembles into oligomeric structures. Using single-particle cryo-electron microscopy, we have determined low-resolution structures of a VacA dodecamer and heptamer, as well as a 3.8-Å structure of the VacA hexamer. These analyses show that VacA p88 consists predominantly of a right-handed beta-helix that extends from the p55 domain into the p33 domain. We map the regions of p33 and p55 involved in hexamer assembly, model how interactions between protomers support heptamer formation, and identify surfaces of VacA that likely contact membrane. This work provides structural insights into the process of VacA oligomerization and identifies regions of VacA protomers that are predicted to contact the host cell surface during channel formation.

Introduction

Helicobacter pylori is a gram-negative bacterium that persistently colonizes the stomachs of >50% of the human population, resulting in a gastric mucosal inflammatory response. While most *H. pylori*-positive individuals remain asymptomatic, *H. pylori* is the strongest known risk factor for development of gastric adenocarcinoma and contributes to the pathogenesis of peptic ulcer disease and gastric lymphoma [1,2]. Gastric cancer is the third leading cause of cancer-related death worldwide, and the World Health Organization has classified *H. pylori* as a type 1 carcinogen [3–5].

There is a high level of genetic diversity among *H. pylori* strains from unrelated individuals, and strain-specific variation in the production of secreted proteins is an important factor that determines whether or not symptomatic disease develops [6–10]. One secreted *H. pylori* protein is vacuolating cytotoxin A (VacA), named for its ability to induce vacuolation in cultured eukaryotic cells [11]. VacA can cause a wide range of cellular alterations in addition to cellular vacuolation, including cell death, depolarization of membrane potential, mitochondrial dysfunction, autophagy, activation of mitogen-activated protein kinases, inhibition of T-cell activities, and other immunomodulatory changes (reviewed in Ref. [12]).

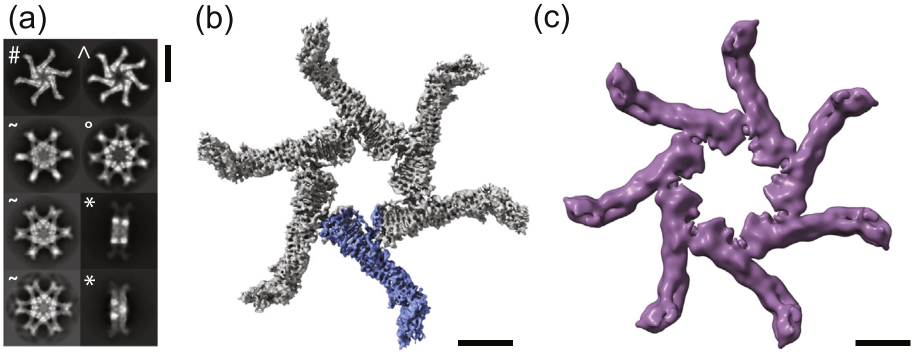

Fig. 1. Cryo-EM analysis of VacA s1m1 oligomers. (a) Representative 2D class averages of VacA oligomer particles. The scale bar represents 20 nm. #, *en face* hexamer 2D class; ^, *en face* heptamer 2D class; ~, *en face* dodecamer 2D classes; °, *en face* tetradecamer 2D class; *, side view of double-layer oligomer 2D classes. (b) 3.8-Å cryo-EM density map of hexameric VacA. One p88 protomer is colored blue. The scale bar represents 50 Å. (c) 8.5-Å resolution cryo-EM density map of heptameric VacA. The scale bar represents 50 Å.

VacA is secreted from *H. pylori* as an 88-kDa monomer (p88), which shares very little sequence similarity to any characterized proteins from other bacterial species. The toxin can undergo limited proteolysis to yield a 33-kDa N-terminal fragment (p33) and a 55-kDa C-terminal fragment (p55) [13]. Regions within both domains contribute to VacA binding to cells [10,14–18]. Experiments with intracellularly expressed toxin show that the minimum portion of VacA required for cell-vacuolating activity contains p33 and 110 amino acids within p55 (residues 1–422) [19]. The sequence of VacA is variable in three polymorphic regions; an N-terminal signal region (s1 or s2) [6], an intermediate region (i1 or i2) located near the C-terminus of p33 [10], and a p55 mid-region (m1 or m2) [6,14]. Sequence variation in all three regions influences the capacity of VacA to cause cellular alterations [14–16,20,21]. Humans infected with *H. pylori* strains that secrete s1/i1/m1 forms of VacA have an increased risk of developing peptic ulcer disease or gastric cancer compared to those infected with *H. pylori* strains secreting s2/i2/m2 forms of VacA [6–10].

Planar lipid bilayer experiments and patch clamping experiments have shown that VacA can form anion-selective membrane channels [22–26]. Mutant forms of VacA defective in channel formation are defective in cell-vacuolating activity [27,28]. Most cellular alterations caused by VacA are attributed to membrane channel formation, either in the plasma membrane or in the membranes of endosomes or lysosomes [22–24,26,29,30].

The 88-kDa VacA monomers secreted by VacA can assemble into an assortment of water-soluble oligomeric structures, including hexamers, heptamers, dodecamers, and tetradecamers [31–35]. Mutant forms of VacA that are defective in oligomerization are also defective in cell-vacuolating activity, and dominant negative mutant forms of VacA can inhibit the activity of wild-type VacA through a process that involves formation of mixed oligomers [27,29,30]. These data suggest that oligomerization is required for VacA toxin activity. Water-soluble oligomeric forms of VacA are presumed to be structurally related to the membrane channels formed by VacA [22,26,33,36]. Water-soluble VacA predominantly organizes into double-layered oligomeric structures, whereas membrane-bound VacA predominantly organizes into hexameric oligomers, with some heptamers also present [37]. Comparison of the two-dimensional (2D) averages of membrane-bound and soluble VacA hexamers generated using negative stain single-particle electron microscopy reveals a structural difference in the central region of the oligomers (corresponding to the p33 region), suggesting that membrane association triggers a structural change in the N-terminus of VacA [37].

A 2.4-Å crystal structure of the majority of p55 (residues 355–811) showed that this region is composed predominantly of a right-handed beta-helix, a structural arrangement adopted by passenger domains of many proteins secreted by type V secretion systems in gram-negative bacteria [38]. A lower-resolution (4.2 Å) crystal structure of a non-oligomerizing VacA mutant protein (VacA Δ346–347) showed that this structural fold extends at least partway into p33 [39]. Low-resolution structures of different oligomer types using negative stain EM have confirmed that p55 is in the peripheral "arm" region of the oligomers and p33 is located toward the center of the oligomeric structure [34,35]. An N-terminal hydrophobic region containing multiple GXXXG motifs, required for toxin activity and membrane channel formation, localizes within a central region of the oligomers and likely corresponds to the channel of VacA membrane pores [27,28]. While it is known that deletion of p33 residues 49–57 and p55 residues 346–347 ablates VacA oligomerization [29,30], there is currently no structural model for how VacA oligomerizes and how different oligomeric states are accommodated. In addition, although there are negative stain 2D averages of VacA bound to membranes [37], there is no three-dimensional (3D) model for how VacA interacts with membrane. In the current study, we use single-particle cryo-electron microscopy (cryo-EM) to determine a 3.8-Å structure of a VacA s1/i1/m1 hexamer and lower resolution structures of a VacA heptamer (8.5 Å) and dodecamer (12 Å). These structures provide molecular insights into how VacA oligomerizes and interacts with membranes, two requirements for its cellular activity.

Results

Cryo-EM reconstruction of VacA oligomers

To investigate the structural basis of VacA oligomerization, we purified wild-type s1/i1/m1 VacA secreted by *H. pylori* and analyzed the protein by single-particle cryo-EM (Fig. SI1a). Similar to what was observed in negative stain using random conical tilt and cryo-negative stain methods [34,35], 2D averages of VacA in vitrified ice showed a mixture of oligomers including hexamers, heptamers, dodecamers, and tetradecamers (Fig. 1a). In vitrified ice, hexamers and dodecamers are the most prevalent oligomer in the sample (~77%), with heptamers and tetradecamers making up the rest of the particles (23%) (Fig. SI2). Just as was seen in negative stain and cryo-negative stain [35], the dodecamers clearly adopt multiple conformations (Fig. 1a). While we determined a 3D structure of a VacA dodecamer (Fig. SI1b), the structural heterogeneity of the dodecamers limited the resolution to ~12 Å (Fig. SI1c).

In the presence of membrane, VacA organizes into single layers (hexamers and heptamers) [37]. Therefore, we were interested in determining structures of soluble single-layered VacA oligomers. While there were *en face* views of hexamers and heptamers in the data set (Fig. 1a), the side views were not easily visible. In addition, although there are clearly 2D averages showing side views of dodecamers and tetradecamers (Fig. 1a, classes labeled with “*”), it is not possible by eye alone to differentiate side views of dodecamers and tetradecamers. Previous studies either proposed [33] or showed [34] that double-layer VacA oligomers (dodecamers or tetradecamers) were formed by the apposition of two face-to-face hexamers or heptamers with a free plane of rotation. For this reason, to determine the structure of a hexamer and heptamer we focused on the 2D averages corresponding to side views of the dodecamers and/or tetradecamers and used particle signal subtraction to remove the signal from one half of the double-layer of each particle. The signal subtracted side-view images were then combined with either the *en face* views of hexamers or heptamers and then classified and aligned in three dimensions (3D). This led to low-resolution structures of a hexamer and heptamer that were then further refined using RELION and cisTEM [40,41] (Fig. SI2). While the arms of the oligomers appear symmetrical even with no symmetry imposed, the densities in the central regions are less defined and do not appear to be well structured (Fig. SI3a). With no symmetry enforced, the average resolution of the VacA hexamer was 8.3 Å (Fig. SI3c). After imposing 6-fold symmetry during the final 3D refinement steps, the global resolution of the 3D reconstruction was 3.8 Å (Fig. 1b; Fig. SI4a; Movie SI1). We also determined a 3D structure of a heptamer using a similar approach (Figs. SI2 and Fig. SI4a). The 8.5-Å resolution density of the heptamer is shown in Fig. 1c. The orientations of the particles found in each structure and the local resolution map of the hexamer with applied 6-fold symmetry are shown in Fig. SI4b–d. We have colored one p88 in the VacA hexamer to highlight how individual protomers are organized in the oligomer. Interestingly, a density extends from p55 of each protomer to contact the adjacent protomer (Fig. 1b).

Structure of VacA p88

The p88 protomers in the 3.8-Å cryo-EM density map of the VacA hexamer are composed of a straight stretch of rolling β-strands extending from the middle of the oligomer and ending in a “hook-shaped” tip (Fig. 1b). From the 2.4-Å crystal structure of p55 [amino acid (a.a.) 355–811, PDB 2QV3] and negative stain 3D maps of a VacA Δ6–27 mutant protein [34,35,38], we know that the VacA C-terminus is located in the “hook-shaped” periphery of the hexamer arms, while the N-terminus is located in the center of the oligomer. The 3.8-Å map of the VacA hexamer allows us to visualize individual β-strands in each protomer (Fig. 1b); however, the resolution is not high enough to confidently define the register of amino acids directly from the map. For this reason, we were not able to build a near-atomic model of p88 *de novo*. There are two available high-resolution structures of portions of VacA: (1) a 2.4-Å crystal structure of a majority of p55 that mapped residues 355–811 [38] and (2) a 4.2-Å crystal structure of VacA Δ346–347, a non-oligomerizing mutant, where residues 348–811 were mapped into the density and additional 165 residues mainly from the p33 domain were built into the electron density [39]. Combining the mapped residues in these structures allowed for the generation of a VacA model containing residues 348–811 and an alanine backbone for an additional 165 residues. We docked this model into a protomer of the 3.8-Å cryo-EM map

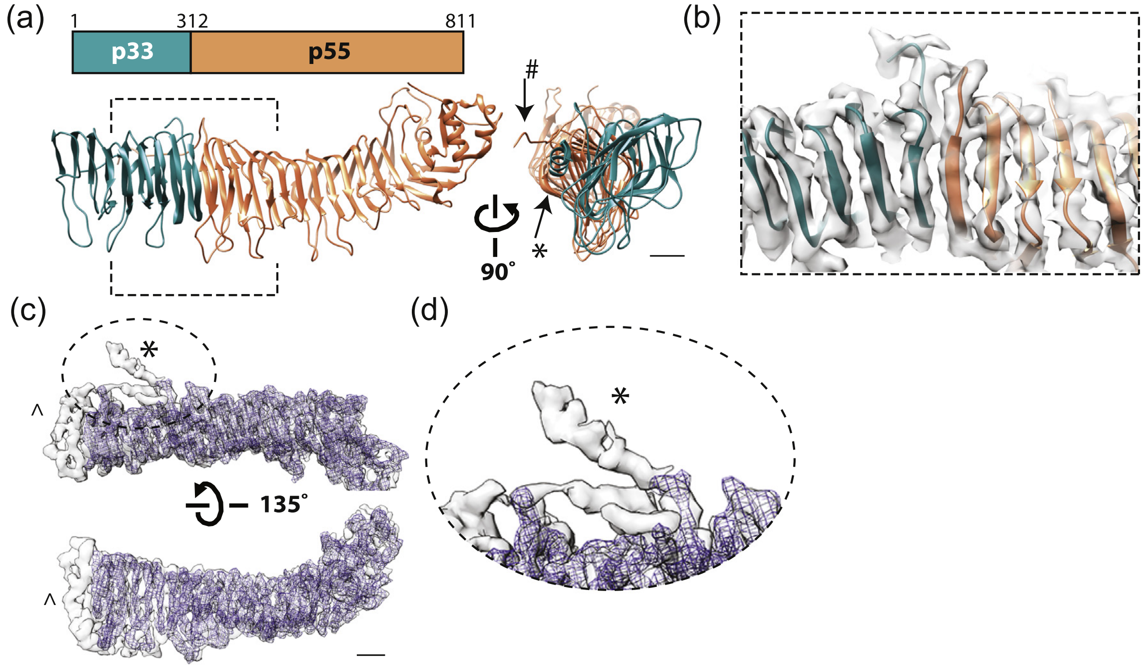

Fig. 2. Structure and interactions of VacA p88. (a) Schematic diagram of VacA p88 monomer subdivided into the p33 (dark cyan) and p55 (coral) domains. Ribbon representation of VacA p88 model. Dashed brackets show the region of the map shown in panel b. Arrow shows direction and degrees of rotation. #, marks the density that extends from the p55 domain and interacts with an adjacent protomer. *, marks position of the alpha-helix. The scale bar represents 10 Å. (b) Closer view of a portion of the p88 model and the density map shows the clear beta-strand separation. (c) Overlay of the density of one p88 protomer extracted from the hexamer density (gray) and the crystal structure of VacA Δ346–347 (blue mesh) [39]. Arrow shows direction and degrees of rotation. Dashed oval shows the regions of the maps shown in panel d. The scale bar represents 10 Å. (d) Closer view of a portion of the p88 map (gray) and VacA Δ346–347 crystal structure (blue mesh). (c–d) ^, marks the p33 region with additional beta strands. *, marks the position of density that extends from the p55 domain and interacts with an adjacent protomer.

of the hexamer using the program Phenix [42]. We were then able to build an additional 65 alanine residues into the cryo-EM density map, including a prominent α-helix that sits perpendicular to the β-strands located in the p33 region and a string of residues that extends from p55 to contact an adjacent protomer (Fig. 2a, c–d).

The model from our cryo-EM analysis shows that the structure of VacA is composed predominantly of rolling β-strands connected by flexible loops (Fig. 2a, b). Combining the crystal structures with the cryo-EM density map, the p55 domain can be traced from threonine 811 (T811) to glutamine 340 (Q340) (Fig. 2a). We could not determine the sequence of the three additional beta-strands that make up an additional turn in the beta-helix visible in the p33 domain, so these are modeled as an alanine backbone. In total, ~115 amino acids are missing in the VacA model built from the 3.8-Å cryo-EM map of a VacA hexamer. We predict that these residues are located in flexible loop regions, as well as in the unstructured density seen in the center of the C1 3D reconstruction (Fig. SI3a). We overlaid the density of one p88 promoter extracted from the hexamer density and the crystal structure of VacA Δ346–347 to compare these structures (Fig. 2c, d). The biggest differences between the VacA hexamer cryo-EM map and the crystal structure of VacA Δ346–347 are the presence of density extending from p55 (a.a. 340–348) that contacts the next protomer, better resolved β-strands extending into the p33 region, and a better defined α-helix positioned where the VacA protomers interact (Fig. 2c, d).

VacA oligomerization is mediated by p33–p55 interactions of neighboring protomers

The 3.8-Å resolution cryo-EM structures of the soluble VacA hexamer allow us to structurally define the points of interaction between the "arms" of VacA protomers. In the VacA hexamer, p88–p88 interactions are mediated by residues in both the p33 and p55 regions (Fig. 3a). Each protomer–protomer interaction involves contacts between one surface in protomer 1 and two surfaces in protomer 2 (Fig. 3a, b). In protomer 1, the major region of interaction is in the part of the density map that contains some beta-sheet elements; however, we cannot predict which residues are involved other than that these residues are within the p33 domain (Fig. 3a, b). In protomer 2, there are two major regions involved in protomer–protomer

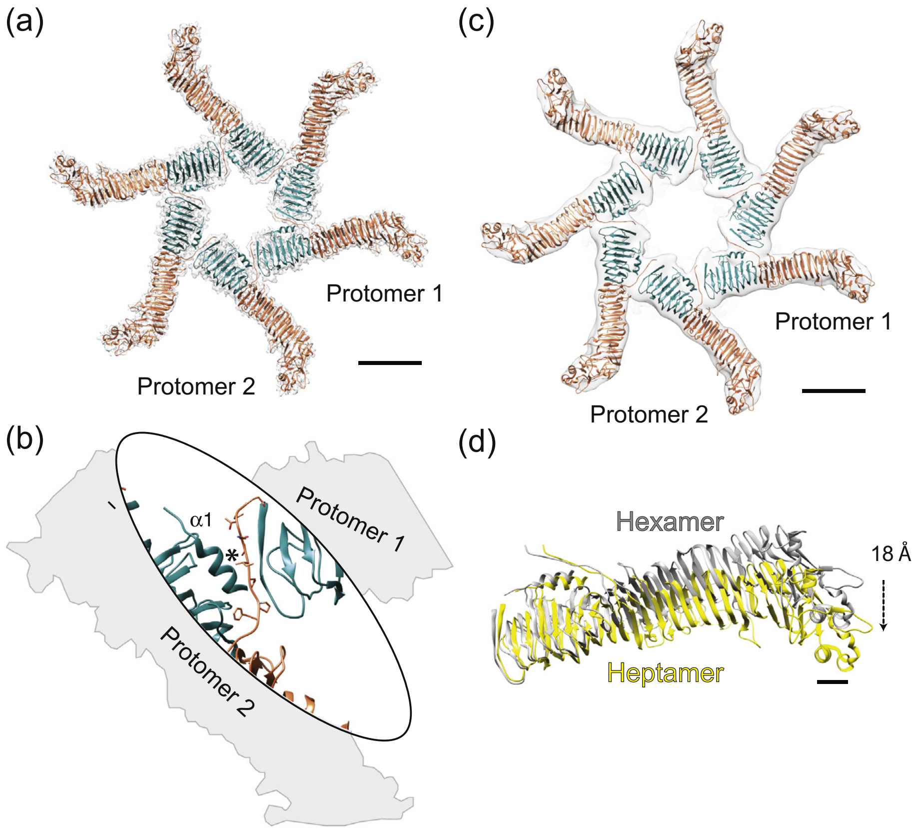

Fig. 3. Comparison of VacA hexamer and heptamer. (a) Envelope of the density of the 3.8-Å hexamer structure (gray) fitted with six p88 ribbon models. Dark cyan, p33 domain; coral, p33 domain. The scale bar represents 50 Å (b) Enlarged view of the interaction interface between protomer 1 and 2. The continuation of the cryo-EM density is traced in gray. The position of residues 346 and 347 in protomer 2 is marked with an *. These residues are part of the p55 extension that contacts the adjacent protomer. (c) Envelope of the density of the 8.5-Å heptamer structure (gray) fitted with seven p88 ribbon models. Dark cyan, p33 domain; coral, p55 domain. The scale bar represents 50 Å. (d) The superposition of the p88 map in protomer 1 of the hexamer (gray) with the p88 map in protomer 1 of the heptamer (yellow) shows the change of angle at the C-terminus of p88. The arrow indicates the direction of the 18 Å shift between protomers in the hexamer and heptamer. The scale bar represents 10 Å.

interactions that include (1) the short α-helix that sits perpendicular to p33 beta strands and (2) residues 340–348, which extend from a beta strand in the p55 density (Fig. 3a, b).

In order to understand the difference between p88 protomer interactions in hexamers *versus* heptamers, we docked the VacA p88 map built using the 3.8-Å VacA hexamer density into the protomers of the 8.5-Å VacA heptamer (Fig. 3c). The p88 map built from the hexamer was able to fit directly into the “arms” of the heptamer, indicating that p88 does not undergo any major conformational changes that depend on the type of oligomer. Similar to what was observed in the hexamer, heptamer protomer–protomer interactions are mediated by one major region in p33 from protomer 1; however, in protomer 2, the angle of the two major contact regions has slightly changed (Fig. 3c, d). This small change in angle at the binding surfaces leads to a shift in protomer angle that propagates into an ~18-Å displacement of each protomer at the p88 C-terminal tip of the heptamer when compared to the hexamer (Fig. 3d).

Model of VacA dodecamer predicts p88 regions that bind membrane

It has been proposed that soluble VacA dodecamers and tetradecamers form as a result of interactions between surfaces of hexamers or heptamers that would normally interact with the lipid membrane and/or cellular receptors if they were present [33,37]. This model is supported by negative stain EM analysis that shows that VacA organizes on membranes as mostly hexamers with some heptamers [37], as well as single-channel and computational modeling studies that suggest chloride channels are formed by hexameric VacA [24,43]. To more clearly define the VacA regions involved in double-layer oligomer formation, and thus also the

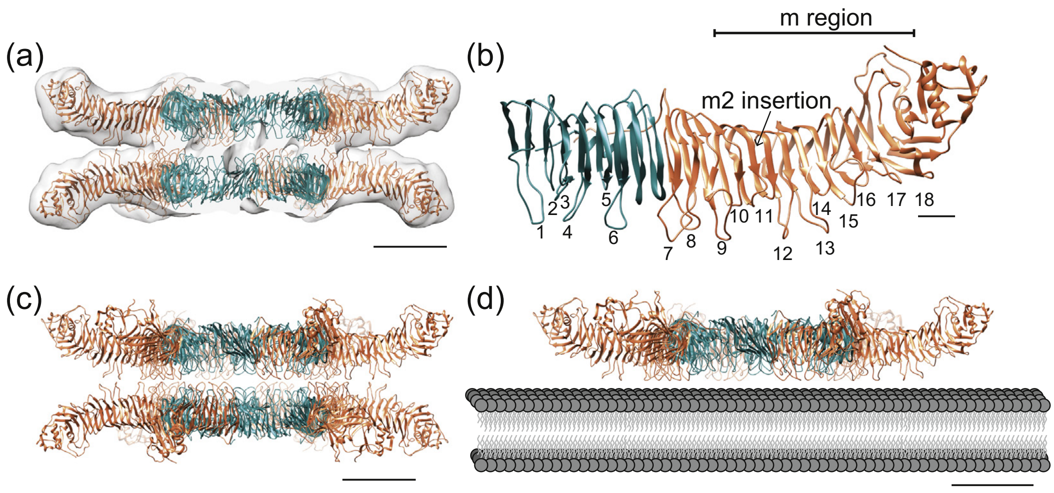

Fig. 4. Model for VacA interactions in dodecamers and on membrane. (a) Central slice view of the envelope of the cryo-EM density map of a VacA dodecamer (gray) fitted with 2 identical models of VacA hexamers (total of 12 p88 models). Dark cyan, p33 domain; coral, p55 domain. The scale bar represents 50 Å. (b) Ribbon diagram of p88 model. Loops that potentially mediate interactions between the two layers of the dodecamer are numbered. The general position of the m-region is marked by brackets. p33 domain in dark cyan, and p55 domain in coral. An arrow marks the position where about 23 m2-specific residues would be inserted if present [6,15]. The scale bar represents 10 Å. (c) Similar view as in panel a, but without the envelope of the cryo-EM density. (d) Model of how a VacA hexamer would sit on a host cell membrane. The same loop regions that interact in the double-layer oligomer are predicted to interact with host cell membranes. Dark cyan, p33 domain; coral, p55 domain. The scale bar represents 50 Å.

regions important for interacting with the lipid bilayer and/or cellular receptors, we fit two identical models of the VacA hexamer into the low-resolution VacA dodecamer map (Fig. 4a). The VacA hexamers fit directly into the VacA dodecamer, without any detectable structural differences at the 3.8-Å resolution of our map. However, it is possible that there are differences when comparing the central region of the hexamer and the central region of the dodecamer (and correspondingly, there may be differences when comparing the central region of the heptamer and the central region of the tetradecamer). The existence of differences in the central region of single-layer and double-layer hexamers–dodecamers (or heptamers–tetradecamers) may be one of the reasons we do not see structured density in the center of the oligomers. The model shows that dodecamers form through interactions between two hexamers, predicted to be mediated by 18 loop regions extending from the β-helix strands in both the p55 and p33 regions (Fig. 4b, c).

VacA contains three polymorphic regions (known as s, i, and m regions). Amino acids within the intermediate region (i1 or i2) located near the C-terminus of p33 and within a middle region (m1 or m2) in p55 are predicted to be involved in receptor binding and/or cellular tropism [6,10,14]. The amino acids that encompass the m-region have not been precisely defined, but span from approximately amino acids 460–736 [6,15]. The position of the m region is shown in Fig. 4b, with brackets and an arrow marking the position where a cluster of about 23 amino acids would be inserted in some m2 forms of VacA [15,44]. We predict that the loops and strands involved in interactions between the two layers of the dodecamer are involved in interactions with cellular membranes and that the corresponding loops and strain variations found in the i- and m-regions are particularly important in making contacts with lipids and/or receptors, thereby influencing toxin activity and cellular tropism (Fig. 4d).

Discussion

We have presented a 3.8-Å structure of a VacA hexamer that provides molecular insights into how soluble VacA oligomerizes and predicts regions of VacA that interact with cellular membranes. The structure shows that VacA is composed mostly of rolling beta-strands connected by flexible loops. The protomers interact through residues in both the p33 and p55 regions. These include an alpha-helix sandwiched between protomers and an extended p55 loop from one protomer that contacts the p33 region from an adjacent protomer. Our structural analysis also shows that a major difference between hexamers and heptamers is the angle of protomer–protomer interactions, with the binding interface between protomers in hexamers being larger than the binding interface supporting heptamers. This difference in binding areas helps explain previous observations that dodecamers and hexamers are more abundant in solution than heptamers and tetradecamers [35].

The model built from our cryo-EM density map shows a number of structural differences compared to the crystal structure of the non-oligomerizing mutant [39]. These include the presence of density extending from p55 (a.a. 340–348) that contacts the adjacent protomer, a better-defined alpha helix that sits between protomers, and better definition of three additional beta strands in p33. These differences may simply reflect the use of two disparate methodologies for structural analysis, or alternatively, some of the differences may reflect structural changes associated with VacA oligomerization, especially the difference involving a strand of residues that extends from p55 and contacts the neighboring protomer.

VacA must oligomerize and insert into the lipid bilayer to form ion channels [22,26,33,36]. It has been proposed that double-layer oligomers found in solution result from interactions between the surfaces of p88 molecules that would contact host cell membranes [33]. Therefore, we predict that the loop and beta-strand regions that make contact in the dodecamer represent the same regions of VacA that interact with cellular membranes (Fig. 4d). Sequence variations among VacA proteins in both the p33 (i1 and i2) and p55 (m1 and m2) domains influence the cellular tropism and toxicity of VacA [6,10,14], likely due to altering the ability of the toxin to bind cellular receptors and/or lipids. We localized the m-region in the cryo-EM map and found that the sequence variations are not confined to individual loops or beta strands (Fig. 4b); however, it is likely that sequence variations, especially deletions and insertions, alter the loops that interact with the surface of the cell. The repeating beta-strand loop–beta-strand pattern of most of VacA also helps explain why it has been difficult to inhibit VacA binding to lipid bilayers. Our model predicts that approximately 18 loops could contact the cell membrane and thus the combined contribution of these protein–lipid interactions along the length of p88 increases the avidity of p88 binding to membrane. In summary, these structures provide new insights into the basis of VacA oligomerization and define regions that are likely important for VacA interactions with cell membranes, two functions that are each required for VacA activity.

Materials and Methods

H. pylori VacA s1m1 expression and purification

The VacA s1m1 protein analyzed in this study is an oligomeric form of the protein that contains a strep tag at residue 808 [39]. The VacA protein was purified from culture supernatant of a genetically modified strain of *H. pylori* strain 60190, as described previously [39].

Cryo-EM

Three microliters of wild-type VacA s1m1 was loaded onto glow-discharged QUANTIFOIL R2/2 200 mesh grids (EMS) and vitrified using a Vitrobot (FEI, Mark IV). In the first session of data collection, the samples were visualized at liquid nitrogen temperature on a Polara electron microscope (Thermo Fisher Scientific) operating at 300 kV. Cryo-EM images were recorded at a nominal magnification of 40,109× using a K2 Summit direct electron detector (Gatan) in counted mode, corresponding to a pixel size of 1.25 Å per pixel with a dose rate of ~6.0 electrons $Å^{-2}$ s^{-1}. In the second session of data collection, the samples were imaged on a Titan Krios electron microscope (Thermo Fisher Scientific) operating at 300 kV. Images were recorded at a nominal magnification of 50,000× using a K2 Summit direct electron detector in counted mode, corresponding to a pixel size of 1.01 Å per pixel with a dose rate of ~6.0 electrons $Å^{-2}$ s^{-1}.

Image processing

Movie frames were first aligned and does-weighted using Motioncor2 [45]. The contrast transfer function (CTF) values were determined using CTFFIND4 [46]. Image processing was carried out using CryoSPARC [47], RELION (v1.4 and 2.0), and cisTEM [40,41,48,49]. A total of 16,462 and 5,471 cryo-EM images were recorded using a Titan Krios and Polara (Thermo Fisher Scientific), respectively (Fig. SI2). The 3D VacA dodecamer was calculated using data collected on the Polara using RELION for 2D classification, *ab initio* model calculation, and 3D refinement with C1 symmetry in the initial rounds and C6 symmetry applied in the final rounds with C6 symmetry. The final resolution of the VacA dodecamer was 12-Å.

Using automated particle picking in RELION, particles were identified and extracted from dose-weighted micrographs. For the hexamer and heptamer 3D reconstructions, the images from the Polara and Titan Krios were combined for all data processing steps. In order to combine the images, particle images extracted from Titan Krios images were down sampled to a pixel size of 1.25 Å match the sampling of images collected on the Polara for data combination. A data set of ~500,000 particles were extracted. Two-dimensional (2D) classifications were performed using RELION-2 (Fig. SI2a). Initial 3D models of the hexamer and the heptamer were generated as follows. Classes representing the *en face* views of hexamers and heptamers, and side views of double-layer oligomers were selected and combined (133,827 particles) (Fig. SI2b). These particles were moved to CryoSPARC for *ab initio* model calculation of either a hexamer or heptamer using no applied symmetry (C1). A 3D hexamer and heptamer were chosen for use as the initial model for homogenous refinement in CryoSPARC using C6 for the hexamer refinement or C7 for the heptamer refinement (Fig. SI2a). Hexamer, heptamer, and double-layer side views were combined and a round of heterogenous refinement with no applied symmetry (C1) was done in CryoSPARC.

The best-defined 3D hexamer and heptamer models were chosen for further refinement and signal subtraction in RELION (Fig. SI2c). 77% of the particles were found in the 3D model of the hexamer, and 23% of the particles were found in the 3D model of the heptamer (Fig. SI2c). The models were then used in RELION for 3D refinement with either C6 or C7 applied symmetry, after which signal subtraction was used on each layer of the double-layer side views to subtract one layer and leave one layer remaining (Fig. SI2c). Signal subtracted images of the side views were then combined with either the *en face* views of the hexamers or heptamers (Fig. SI2d). Next supervised refinement in RELION was done with no applied symmetry (C1), and then the final 3D refinement was done using cisTEM (Fig. SI2d). The final resolution of the VacA hexamer and heptamer was 3.8 and 8.5 Å, respectively. Reported resolutions are based on the gold standard Fourier shell correlation (FSC) using the 0.143 criterion [50]. The FSC curve for the hexamer (Fig. SI4A) oscillates in the range of 5- to 7-Å resolution, with a correlation score dropping to around 0.55. The typical spacing of beta-strands in the VacA structure is around 6 Å. It is likely that the FSC curve oscillation seen in Fig. SI4a is related to p88 being dominated by beta strands. High-resolution noise substitution was used to correct for the effects of soft masking on the FSC curves. Local resolution was determined using ResMap [51].

Model building, structure refinement, and validation

The models of the VacA p55 domain (2QV3 [38]) and Δ346–347 VacA non-oligomerizing mutant [39] were docked into one protomer of the 3.8-Å VacA hexamer cryo-EM density map using the Phenix Dock in map tool, and coordinates were exported to COOT [52,53]. The model was then extended in COOT [52]. The final model was obtained by iterative cycles of manual model refinement in COOT and refinement with Real-space refinement in the Phenix suite of programs [42,53]. During refinement, the PDB 2QV3 was used as a reference model. Secondary structure was predicted from the polyalanine model using Phenix.secondary_structure_restraints with the CaBLAM search method [54] and used as refinement restraints. Phenix Map Symmetry was used to determine the symmetry of the map. The Phenix Apply NCS operators tool was used to transform the p88 model into the six arms of the hexamer to generate a complete structure. A final Real-space refinement was completed on the hexamer model. Validation of the model was performed using the Comprehensive Validation (cryo-EM) tool in Phenix (Table SI1). FSC curves were calculated for the model in relation to half-map 1 and compared with that for the summed map (Fig. SI5). Programs used for structure determination and refinement were accessed through SBGrid [55]. Figures were prepared with Chimera and ChimeraX [56,57].

CRediT authorship contribution statement

Min Su: Investigation, Data curation, Formal analysis, Writing - review & editing. **Amanda L. Erwin:** Investigation, Data curation, Visualization, Formal analysis, Writing - original draft, Writing - review & editing. **Anne M. Campbell:** Investigation. **Tasia M. Pyburn:** Investigation, Formal analysis. **Lauren E. Salay:** Investigation, Validation. **Jessica L. Hanks:** Investigation. **D. Borden Lacy:** Validation, Visualization, Writing - review & editing. **David L. Akey:** Validation, Visualization. **Timothy L. Cover:** Conceptualization, Formal analysis, Funding acquisition, Investigation, Writing - original draft, Writing - review & editing. **Melanie D. Ohi:** Conceptualization, Formal analysis, Funding acquisition, Investigation, Writing - original draft, Writing - review & editing.

Data availability

The cryo-EM volumes have been deposited in the Electron Microscopy Data Bank under accession codes EMD-20024 (hexamer) and EMD-20029 (heptamer). Model coordinates have been deposited in the Protein Data Bank under accession number 6ODY.

Supplementary data to this article can be found online at https://doi.org/10.1016/j.jmb.2019.03.029.

Acknowledgments

We thank the Cianfrocco, Cover, Lacy, and Ohi laboratories for helpful discussions. We acknowledge the use of the U-M LSI cryo-EM facility, managed by M. Su and A. Bondy, and U-M LSI IT support. This work was supported by the National Institutes of Health(AI039657, CA116087, T32CA119925, T32GM08320, R35GM118089, and F31AI112324) and the Department of Veterans Affairs (1I01BX004447).

Received 22 March 2019;
Received in revised form 29 March 2019;
Accepted 29 March 2019
Available online 5 April 2019

Keywords:
single-particle cryo-EM;
pore-forming toxins;
gastric cancer

Co-first authors.

Abbreviations used:
VacA, vacuolating cytotoxin A; cryo-EM, cryo-electron microscopy; FSC, Fourier shell correlation.

References

[1] B.J. Marshall, C.S. Goodwin, J.R. Warren, R. Murray, E.D. Blincow, S.J. Blackbourn, et al., Prospective double-blind trial of duodenal ulcer relapse after eradication of *Campylobacter pylori*, Lancet. 2 (1988) 1437–1442.

[2] S. Suerbaum, P. Michetti, *Helicobacter pylori* infection, N. Engl. J. Med. 347 (2002) 1175–1186.

[3] C.S. Fuchs, R.J. Mayer, Gastric carcinoma, N. Engl. J. Med. 333 (1995) 32–41.

[4] C. de Martel, J. Ferlay, S. Franceschi, J. Vignat, F. Bray, D. Forman, et al., Global burden of cancers attributable to infections in 2008: a review and synthetic analysis, Lancet Oncol. 13 (2012) 607–615.

[5] Anonymous, Schistosomes, Liver Flukes and *Helicobacter pylori* IARC Monographs on the Evaluation of Carcinogenic Risks to Humans, International Agency for Research on Cancer, Lyons, France, 1994.

[6] J.C. Atherton, P. Cao, R.M. Peek Jr., M.K. Tummuru, M.J. Blaser, T.L. Cover, Mosaicism in vacuolating cytotoxin alleles of *Helicobacter pylori*. Association of specific vacA types with cytotoxin production and peptic ulceration, J. Biol. Chem. 270 (1995) 17771–17777.

[7] T.L. Cover, *Helicobacter pylori* diversity and gastric cancer risk, mBio. 7 (2016).

[8] C. Figueiredo, J.C. Machado, P. Pharoah, R. Seruca, S. Sousa, R. Carvalho, et al., *Helicobacter pylori* and interleukin 1 genotyping: an opportunity to identify high-risk individuals for gastric carcinoma, J. Natl. Cancer Inst. 94 (2002) 1680–1687.

[9] A.A. Memon, N.R. Hussein, V.Y. Miendje Deyi, A. Burette, J. C. Atherton, Vacuolating cytotoxin genotypes are strong markers of gastric cancer and duodenal ulcer-associated *Helicobacter pylori* strains: a matched case–control study, J. Clin. Microbiol. 52 (2014) 2984–2989.

[10] J.L. Rhead, D.P. Letley, M. Mohammadi, N. Hussein, M.A. Mohagheghi, M. Eshagh Hosseini, et al., A new *Helicobacter pylori* vacuolating cytotoxin determinant, the intermediate region, is associated with gastric cancer, Gastroenterology. 133 (2007) 926–936.

[11] T.L. Cover, M.J. Blaser, Purification and characterization of the vacuolating toxin from *Helicobacter pylori*, J. Biol. Chem. 267 (1992) 10570–10575.

[12] N.J. Foegeding, R.R. Caston, M.S. McClain, M.D. Ohi, T.L. Cover, An overview of *Helicobacter pylori* VacA toxin biology, Toxins. 8 (2016).

[13] J.L. Telford, P. Ghiara, M. Dell'Orco, M. Comanducci, D. Burroni, M. Bugnoli, et al., Gene structure of the *Helicobacter pylori* cytotoxin and evidence of its key role in gastric disease, J. Exp. Med. 179 (1994) 1653–1658.

[14] C. Pagliaccia, M. de Bernard, P. Lupetti, X. Ji, D. Burroni, T.L. Cover, et al., The m2 form of the *Helicobacter pylori* cytotoxin has cell type-specific vacuolating activity, Proc. Natl. Acad. Sci. U. S. A. 95 (1998) 10212–10217.

[15] X. Ji, T. Fernandez, D. Burroni, C. Pagliaccia, J.C. Atherton, J.M. Reyrat, et al., Cell specificity of *Helicobacter pylori* cytotoxin is determined by a short region in the polymorphic midregion, Infect. Immun. 68 (2000) 3754–3757.

[16] W.C. Wang, H.J. Wang, C.H. Kuo, Two distinctive cell binding patterns by vacuolating toxin fused with glutathione *S*-transferase: one high-affinity m1-specific binding and the other lower-affinity binding for variant m forms, Biochemistry. 40 (2001) 11887–11896.

[17] V.J. Torres, S.E. Ivie, M.S. McClain, T.L. Cover, Functional properties of the p33 and p55 domains of the *Helicobacter pylori* vacuolating cytotoxin, J. Biol. Chem. 280 (2005) 21107–21114.

[18] C. Gonzalez-Rivera, H.M. Algood, J.N. Radin, M.S. McClain, T.L. Cover, The intermediate region of *Helicobacter pylori* VacA is a determinant of toxin potency in a Jurkat T cell assay, Infect. Immun. 80 (2012) 2578–2588.

[19] D. Ye, D.C. Willhite, S.R. Blanke, Identification of the minimal intracellular vacuolating domain of the *Helicobacter pylori* vacuolating toxin, J. Biol. Chem. 274 (1999) 9277–9282.

[20] D.P. Letley, J.C. Atherton, Natural diversity in the N terminus of the mature vacuolating cytotoxin of *Helicobacter pylori* determines cytotoxin activity, J. Bacteriol. 182 (2000) 3278–3280.

[21] M.S. McClain, P. Cao, T.L. Cover, Amino-terminal hydrophobic region of *Helicobacter pylori* vacuolating cytotoxin (VacA) mediates transmembrane protein dimerization, Infect. Immun. 69 (2001) 1181–1184.

[22] D.M. Czajkowsky, H. Iwamoto, T.L. Cover, Z. Shao, The vacuolating toxin from *Helicobacter pylori* forms hexameric pores in lipid bilayers at low pH, Proc. Natl. Acad. Sci. U. S. A. 96 (1999) 2001–2006.

[23] I. Szabo, S. Brutsche, F. Tombola, M. Moschioni, B. Satin, J. L. Telford, et al., Formation of anion-selective channels in the cell plasma membrane by the toxin VacA of *Helicobacter pylori* is required for its biological activity, EMBO J. 18 (1999) 5517–5527.

[24] H. Iwamoto, D.M. Czajkowsky, T.L. Cover, G. Szabo, Z. Shao, VacA from *Helicobacter pylori*: a hexameric chloride channel, FEBS Lett. 450 (1999) 101–104.

[25] F. Tombola, F. Oregna, S. Brutsche, I. Szabo, G. Del Giudice, R. Rappuoli, et al., Inhibition of the vacuolating and anion channel activities of the VacA toxin of *Helicobacter pylori*, FEBS Lett. 460 (1999) 221–225.

[26] F. Tombola, C. Carlesso, I. Szabo, M. de Bernard, J.M. Reyrat, J.L. Telford, et al., *Helicobacter pylori* vacuolating toxin forms anion-selective channels in planar lipid bilayers: possible implications for the mechanism of cellular vacuolation, Biophys. J. 76 (1999) 1401–1409.

[27] A.D. Vinion-Dubiel, M.S. McClain, D.M. Czajkowsky, H. Iwamoto, D. Ye, P. Cao, et al., A dominant negative mutant of *Helicobacter pylori* vacuolating toxin (VacA) inhibits VacA-induced cell vacuolation, J. Biol. Chem. 274 (1999) 37736–37742.

[28] M.S. McClain, H. Iwamoto, P. Cao, A.D. Vinion-Dubiel, Y. Li, G. Szabo, et al., Essential role of a GXXXG motif for membrane channel formation by *Helicobacter pylori* vacuolating toxin, J. Biol. Chem. 278 (2003) 12101–12108.

[29] S.E. Ivie, M.S. McClain, V.J. Torres, H.M. Algood, D.B. Lacy, R. Yang, et al., *Helicobacter pylori* VacA subdomain required for intracellular toxin activity and assembly of functional oligomeric complexes, Infect. Immun. 76 (2008) 2843–2851.

[30] C. Genisset, C.L. Galeotti, P. Lupetti, D. Mercati, D.A. Skibinski, S. Barone, et al., A *Helicobacter pylori* vacuolating toxin mutant that fails to oligomerize has a dominant negative phenotype, Infect. Immun. 74 (2006) 1786–1794.

[31] P. Lupetti, J.E. Heuser, R. Manetti, P. Massari, S. Lanzavecchia, P.L. Bellon, et al., Oligomeric and subunit structure of the *Helicobacter pylori* vacuolating cytotoxin, J. Cell Biol. 133 (1996) 801–807.

[32] S. Lanzavecchia, P.L. Bellon, P. Lupetti, R. Dallai, R. Rappuoli, J.L. Telford, Three-dimensional reconstruction of metal replicas of the *Helicobacter pylori* vacuolating cytotoxin, J. Struct. Biol. 121 (1998) 9–18.

[33] M. Adrian, T.L. Cover, J. Dubochet, J.E. Heuser, Multiple oligomeric states of the *Helicobacter pylori* vacuolating toxin demonstrated by cryo-electron microscopy, J. Mol. Biol. 318 (2002) 121–133.

[34] C. El-Bez, M. Adrian, J. Dubochet, T.L. Cover, High resolution structural analysis of *Helicobacter pylori* VacA toxin oligomers by cryo-negative staining electron microscopy, J. Struct. Biol. 151 (2005) 215–228.

[35] M.G. Chambers, T.M. Pyburn, C. Gonzalez-Rivera, S.E. Collier, I. Eli, C.K. Yip, et al., Structural analysis of the oligomeric states of *Helicobacter pylori* VacA toxin, J. Mol. Biol. 425 (2013) 524–535.

[36] N.A. Geisse, T.L. Cover, R.M. Henderson, J.M. Edwardson, Targeting of *Helicobacter pylori* vacuolating toxin to lipid raft membrane domains analysed by atomic force microscopy, Biochem. J. 381 (2004) 911–917.

[37] T.M. Pyburn, N.J. Foegeding, C. Gonzalez-Rivera, N.A. McDonald, K.L. Gould, T.L. Cover, et al., Structural organization of membrane-inserted hexamers formed by *Helicobacter pylori* VacA toxin, Mol. Microbiol. 102 (1) (2016) 22–36.

[38] K.A. Gangwer, D.J. Mushrush, D.L. Stauff, B. Spiller, M.S. McClain, T.L. Cover, et al., Crystal structure of the *Helicobacter pylori* vacuolating toxin p55 domain, Proc. Natl. Acad. Sci. U. S. A. 104 (2007) 16293–16298.

[39] C. Gonzalez-Rivera, A.M. Campbell, S.A. Rutherford, T.M. Pyburn, N.J. Foegeding, T.L. Barke, et al., A nonoligomerizing mutant form of *Helicobacter pylori* VacA allows structural analysis of the p33 domain, Infect. Immun. 84 (2016) 2662–2670.

[40] S.H. Scheres, RELION: implementation of a Bayesian approach to cryo-EM structure determination, J. Struct. Biol. 180 (2012) 519–530.

[41] T. Grant, A. Rohou, N. Grigorieff, cisTEM, user-friendly software for single-particle image processing, eLife. 7 (2018).

[42] P.V. Afonine, B.K. Poon, R.J. Read, O.V. Sobolev, T.C. Terwilliger, A. Urzhumtsev, et al., Real-space refinement in PHENIX for cryo-EM and crystallography, Acta Crystallogr. D Struct. Biol. 74 (2018) 531–544.

[43] S. Kim, A.K. Chamberlain, J.U. Bowie, Membrane channel structure of *Helicobacter pylori* vacuolating toxin: role of multiple GXXXG motifs in cylindrical channels, Proc. Natl. Acad. Sci. U. S. A. 101 (2004) 5988–5991.

[44] D.A. Skibinski, C. Genisset, S. Barone, J.L. Telford, The cell-specific phenotype of the polymorphic vacA midregion is independent of the appearance of the cell surface receptor protein tyrosine phosphatase beta, Infect. Immun. 74 (2006) 49–55.

[45] S.Q. Zheng, E. Palovcak, J.P. Armache, K.A. Verba, Y. Cheng, D.A. Agard, MotionCor2: anisotropic correction of beam-induced motion for improved cryo-electron microscopy, Nat. Methods 14 (2017) 331–332.

[46] A. Rohou, N. Grigorieff, CTFFIND4: fast and accurate defocus estimation from electron micrographs, J. Struct. Biol. 192 (2015) 216–221.

[47] A. Punjani, J.L. Rubinstein, D.J. Fleet, M.A. Brubaker, cryoSPARC: algorithms for rapid unsupervised cryo-EM structure determination, Nat. Methods 14 (2017) 290–296.

[48] S.H. Scheres, Semi-automated selection of cryo-EM particles in RELION-1.3, J. Struct. Biol. 189 (2015) 114–122.

[49] D. Kimanius, B.O. Forsberg, S.H. Scheres, E. Lindahl, Accelerated cryo-EM structure determination with parallelisation using GPUs in RELION-2, eLife. 5 (2016).

[50] S.H. Scheres, Processing of structurally heterogeneous cryo-EM data in RELION, Methods Enzymol. 579 (2016) 125–157.

[51] L. Swint-Kruse, C.S. Brown, Resmap: automated representation of macromolecular interfaces as two-dimensional networks, Bioinformatics. 21 (2005) 3327–3328.

[52] P. Emsley, K. Cowtan, Coot: model-building tools for molecular graphics, Acta Crystallogr. D Biol. Crystallogr. 60 (2004) 2126–2132.

[53] P.D. Adams, R.W. Grosse-Kunstleve, L.W. Hung, T.R. Ioerger, A.J. McCoy, N.W. Moriarty, et al., PHENIX: building new software for automated crystallographic structure determination, Acta Crystallogr. D Biol. Crystallogr. 58 (2002) 1948–1954.

[54] O.V. Sobolev, P.V. Afonine, P.D. Adams, A. Urzhumtsev, Programming new geometry restraints: parallelity of atomic groups, J. Appl. Crystallogr. 48 (2015) 1130–1141.

[55] A. Morin, B. Eisenbraun, J. Key, P.C. Sanschagrin, M.A. Timony, M. Ottaviano, et al., Collaboration gets the most out of software, eLife. 2 (2013), e01456.

[56] E.F. Pettersen, T.D. Goddard, C.C. Huang, G.S. Couch, D.M. Greenblatt, E.C. Meng, et al., UCSF Chimera—a visualization system for exploratory research and analysis, J. Comput. Chem. 25 (2004) 1605–1612.

[57] T.D. Goddard, C.C. Huang, E.C. Meng, E.F. Pettersen, G.S. Couch, J.H. Morris, et al., UCSF ChimeraX: meeting modern challenges in visualization and analysis, Protein Sci. 27 (2018) 14–25.